



JOURNAL OF
SYNCHROTRON
RADIATION

Volume 28 (2021)

Supporting information for article:

**Calculating Absorption Dose When X-ray Irradiation Modifies
Material Quantity and Chemistry**

Viatcheslav Berejnov, Boris Rubinstein, Lis G. A. Melo and Adam Hitchcock

Supplemental Information for
Calculating Absorption Dose When X-ray Irradiation Modifies Material
Quantity and Chemistry

Viatcheslav Berejnov^{1,#,*}, Boris Rubinstein², Lis G. A. Melo^{3,\$}, and Adam P. Hitchcock³

1. Automotive Fuel Cell Corporation, 9000 Glenlyon Parkway, Burnaby, BC, Canada V5J 5J8

2. Stowers Institute for Medical Research, 1000 East 50th Street, Kansas City, MO 64110, USA

3. Dept. Chemistry and Chemical Biology, McMaster University, Hamilton, ON Canada L8S4M1

* corresponding author: berejnov@gmail.com

current address: FTXT Energy Technology Co., Ltd, Baoding, Hebei, China

\$ current address: Simon Fraser University, Burnaby, Canada

Table S-1 Table of symbols

symbol	meaning	symbol	meaning
Gy	Grey - dose (J/kg)	e_D	Photon energy for creating dose (eV)
D	Dose (in units of Gy)	e_A	Photon energy for analyzing damage (eV)
e	Photon energy variable (eV), when indexed – corresponds to a specific value	n	Index of the absorption edge (element)
θ, t	θ is elapsed time; t is time variable (s)	Δe_-	pre-edge photon energy interval
A	Optical density	Δe_+	post-edge photon energy interval
A_{pre}	Pre-edge absorption	TM	Time multiplier
A_{pst}	Post-edge absorption	a	Elemental atomic array (Bold)
A_i	Array of optical densities (Bold)	σ	Elemental cross-section array (Bold)
M	Mass (kg)	M_r	Array of molecular masses (Bold)
μ	linear absorption coefficient (m ⁻¹)	M_r	effective molecular mass
μ_m	mass absorption coefficient (cm ² .g ⁻¹)	$e_{(-)}, e_{(+)}$	Array of pre (-) or post (+) photon energies (Bold)
σ	Atomic cross-section (10 ⁻²⁴ cm ² /atom)	v	Molar volume (cm ³ .mol ⁻¹)
\dot{E}	Rate of absorbed energy (J/s)	N	Number of moles in volume, sh
x	Integration variable (Eq.1, denotes time)	C	Constant (9.111x10 ⁻³ nm ² .eV ⁻¹)
i	transmitted X-ray intensity (ph/s)	$f(e)$	Imaginary scattering factor
i_o	Incident X-ray intensity (ph/s)	w	amount of material per area unit (mol/cm ²)
ρ	Density (kg/m ³)	c, b	Linear fit coefficients (Eq. 16)
h	Material thickness (m)	B_i	Fit to experimental pre/post spectra of i -th pad (Bold)
s	Cross-sectional area of beam (m ²)	$R_i(A_i, B_i)$	Residual of fit for i -th pad
k	Detector efficiency	MSE	Mean square error
OD	Optical density	D_p	Dose which generating the 9-pad pattern
$OD1$	Optical density for 1 nm, standard density	D_s	Dose associated with post-pad spectroscopy
i	If an index – then it is the pad index	δr	Width (nm) of outermost zone of a zone plate
L_i	linear dose rate (Gy.m ⁻¹ s ⁻¹) for pad i [dose rate = $dD/dt = L*\mu$]	A_o	OSA – sample distance in STXM

$T_{i-1,i}$	Effective time integral (s) from $t-l$ to t	EW	Equivalent weight of PFSA
Δx	Spatial resolution (probe width) (nm)	r	Spatial resolution (nm) of focused beam
τ	Dwell time (s)	N_a	Avogadro's number (6.022×10^{23})

SI 1.1 Development of an expression for obtaining a from the experiment

Once the elemental array a is known, then **Eq. 12** allows to calculate μ_m and then μ (for a given ρ).

$$\mu_m(\text{unit}) = N_a \frac{(\sigma \cdot a)}{(M_r \cdot a)}, \quad (\text{S1})$$

However, we are looking for the opposite – for obtaining the elemental array a by fitting the experimental optical densities of different pads $A(e, t_i)$ (outside of the bonding-dependent near edge fine structure) against the linear absorption coefficient $\mu(e, t_i)$ where the elemental array $a(t)$ is unknown. For this purpose, despite having the correct functionality, **Eq. S1** is not suitable. Indeed, the elemental array a contributes to both scalar products in the numerator and denominator of **Eq. S1**. The array a itself cannot be cancelled, instead any arbitrarily chosen element a_i can be cancelled because the elemental array can be written as $a = a_1(1, a_2/a_1, \dots, a_n/a_1)$ and in this case a_1 can be cancelled in **Eq. S1**. Obviously, a_1 can be substituted by any other arbitrarily chosen a_i . Therefore, using **Eq. S1** for fitting against the particular a will provide only the ratios of the atomic numbers with respect to the dose applied.

We need to convert **Eq. S1 (Eq.12)** into a form suitable for numerical fitting. Expressing the density ρ through the molar volume of the material unit, v , and combining with equation $\mu = \rho\mu_m$, have

$$\mu(e, a(t)) = \rho\mu_m(e, a(t)) = N \frac{(M_r \cdot a)}{sh} N_a \frac{(\sigma \cdot a)}{(M_r \cdot a)}, \quad (\text{S2})$$

After canceling the scalar products $(M_r \cdot a)$ and rearranging it reads

$$\mu(e, a(t)) = (h^{-1}) \frac{N}{s} N_a (\sigma(e) \cdot a(t)) \quad (\text{S3})$$

This equation shows clearly that μ depends on $a(t)$. The only way damage can affect μ is through changes in the elemental array. **Eq. S3 (Eq.13)** has none of the above limitations where the elemental array a is presented in both numerator and denominator, and thus, could be used for developing the fitting approach.

SI 1.2 Numerical framework for obtaining elemental array \mathbf{a}

- 1) The experiment outputs the piecewise array of the optical density functions recorded for the i -th pad:

$$\mathbf{A}_i(\mathbf{e}, t_i) = (A_{1,-}(\mathbf{e}_-, t_i), A_{1,+}(\mathbf{e}_+, t_i), A_{2,-}(\mathbf{e}_-, t_i), A_{2,+}(\mathbf{e}_+, t_i), \dots, A_{n,-}(\mathbf{e}_-, t_i), A_{n,+}(\mathbf{e}_+, t_i)) \quad (\text{S4})$$

where the *pre* (–) and *post* (+) denote the “pieces” or the energy intervals $\mathbf{e}_{(-\text{or } +)} = (e_1, e_2, e_3, \dots)$ for each of n edges taken for the fit.

Each sub-array of the i -th pad for the n -th edge $A_{n,-}(\mathbf{e}_-, t_i)$ or $A_{n,+}(\mathbf{e}_+, t_i)$ may have different number of energy dependent optical density elements corresponding to the experimental data of the particular edge.

- 2) Dimension of the elemental array \mathbf{a} is $n+2$, where n is the number of the elements those edges provide the experimental data for the piecewise array \mathbf{A}_i . For our case $\mathbf{a} = (\text{S}, \text{C}, \text{O}, \text{F}, \text{H})$, $n=3$ and corresponds to C 1s, O 1s, and F 1s edges, respectively. The additional number 2 corresponds in our case to the elements S and H considered theoretically, where S is a variable and H is fixed to 1.
- 3) The numerical fitting is an iterative process. We set some values for the elemental array \mathbf{a} , then calculate **Eq. 16 (S5)** – the simplest generalized version of **Eq.15**,

$$\mathbf{B}_i(\mathbf{e}, \mathbf{a}(t_i)) = c + b(\boldsymbol{\sigma}(\mathbf{e}) \cdot \mathbf{a}(t_i)), \quad (\text{S5})$$

then find residual between the experimental \mathbf{A}_i and calculated \mathbf{B}_i . Once all trials of the elemental array \mathbf{a} are calculated we select those \mathbf{a} arrays which provide the minimal residual within the pre-selected residual interval. The final output of the elemental array \mathbf{a} would be an average of those arrays.

- 4) For the given i -th pad, the array \mathbf{A}_i is created, from the data, and the calculation starts with the arbitrarily set \mathbf{a} , (1,1,1,1,1). Following rule is used for assigning the element-position for the \mathbf{a} and $\boldsymbol{\sigma}$ arrays: *the first position in the array corresponds to Sulfur, second to Carbon, third to Oxygen, forth to Fluorine, and fifth to Hydrogen, respectively.*
- 5) Then, coefficients c and b in **Eq. S5** are calculated by applying the linear least square fit to the data \mathbf{A}_i with respect to the chosen \mathbf{a} and given $\boldsymbol{\sigma}$.
- 6) The quality of the fit is calculated for each iteration and defined by the residual $R_i(\mathbf{A}, \mathbf{B})$. It depends on \mathbf{a} as a parameter. We use the mean square error $MSE(\mathbf{a})$ as metric for the residual $R_i(\mathbf{A}, \mathbf{B}) = MSE_i(\mathbf{a})$. It is defined as a sum with respect to all available photon

energies e_l ($l=1, 2, \dots, N_p$) of all energy intervals of all experimental edges included in array A_i (Eq. S4):

$$MSE_i(\mathbf{a}) = \frac{1}{N_p} \sum_l (A_i(e_l, t_i) - B_i(e_l, \mathbf{a}(t_i)))^2 \quad (\text{S6})$$

here N_p is a total number of the energy points for the all *pre* and *post* edges intervals used for fitting.

- 7) Once $MSE_i(\mathbf{a})$ is calculated the elemental array \mathbf{a} is re-set to new \mathbf{a} , (2,1,1,1,1) and calculation step (5) is repeated. Number of iterations is defined by the number of permutations of the $n+2$ components of the array \mathbf{a} accounting the increment of the change of the \mathbf{a} component values (1.0 or 0.1 depending on the expected accuracy). The following cut-offs for the maximal numbers of atoms in the elemental arrays were chosen S=3, C=30, O=15, F=50. The number of atoms corresponded to the minimal MSE were always less than the cut-off values by $\sim 20\%$, ensuring that the minimum does not correspond to the edge of the variation interval of the atomic numbers.
- 8) After all permutations are used the process stops. Due to the noise, we use few elemental arrays with the lowest $R_i(\mathbf{A}, \mathbf{B}) = MSE_i(\mathbf{a})$ for calculating the average elemental array \mathbf{a} and then for calculating the appropriate c and b . The coefficient $b=w$. The coefficient c is a constant and always small comparing minimal A from the experiment. It is probably emerges to higher order or stray light (photon energies different from e_D) which passes through the ZP, OSA and sample.

SI 2. Detector efficiency

The efficiency of the phosphor-PMT detector was measured using a modified version of the cross-over transition in PMMA lithography (Leontowich, 2012). We found that the detector efficiency can be significantly different (higher or lower) when new detector coatings were applied. The efficiency was also sensitive to the PMT voltage and discriminator settings which were set to ensure that the detector response was saturated. During the period when the data for this paper was acquired (2017-2018) the detector efficiency at 320 eV was $43 \pm 14 \%$ for the CLS ambient STXM microscope (see Fig. S2). The efficiency rises with photon energy to a value at 710 eV of $83 \pm 6 \%$. The dashed curve in Fig. S2 corresponds to the approximation function $k(e) = (-0.0002e^2 + 0.288e - 32.355)/100$.

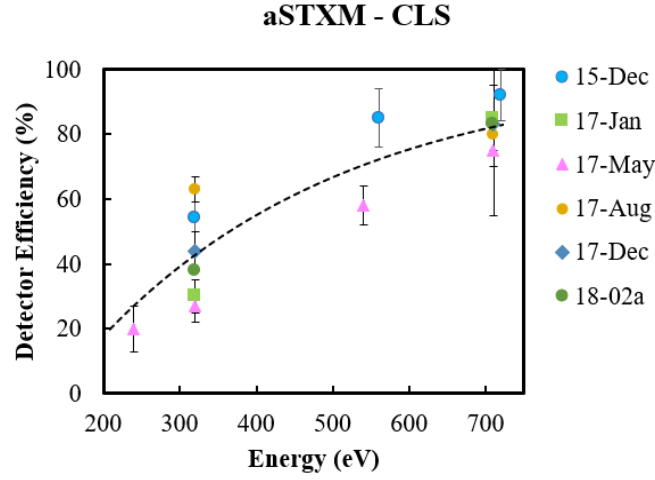


Figure S2: CLS detector efficiencies and approximation with respect to the photon energy.

SI 3.1 Interpolating optical density, $A(t)$

The optical density function, $A(t)$, can be obtained either from an OD-image of the 9-pad pattern recorded at the damage energy, 320 eV in this case (**Fig. 3c**), or from spectra similar to those presented in **Fig. 5a**.

We are using two models to interpolating $A(e_D, t)$ over the full time range. Model 1 uses an exponential interpolation $A(t) = c_1 + a_1 e^{-b_1 t}$. Model 2 uses a hyperbolic interpolation $A(t) = c_2 + \frac{a_2}{b_2 + t}$. **Figure S 3.1** plots fits of the two models to the experimental $A(t)$ data. (a) and (b) correspond to the fit of the exponential model 1 (solid curve), while (c) and (d) to the hyperbolic model 2. Black dots are the raw optical densities at 320eV at each pad. **Table S3.1** presents the fitting coefficients with the mean square error calculated for each model with respect to the given data points of $A(e_D, t)$.

	a	b	c	MSE
model 1	0.15	0.80	0.34	3.0E-04
model 2	0.17	0.94	0.32	9.0E-05

Table S3.1. Least linear fitting coefficients and mean square errors for models 1 and 2

Note, the fitting error for model 1 is three times higher than for model 2. Also note that the last two points in **Fig. S3.1b** are missing because $(A - c_1) < 0$. Indeed, the argument of the Log

function must be positive, i.e. for these two points $A < 0.34$, which is a value of c_1 . Model 2 does not have such a restriction.

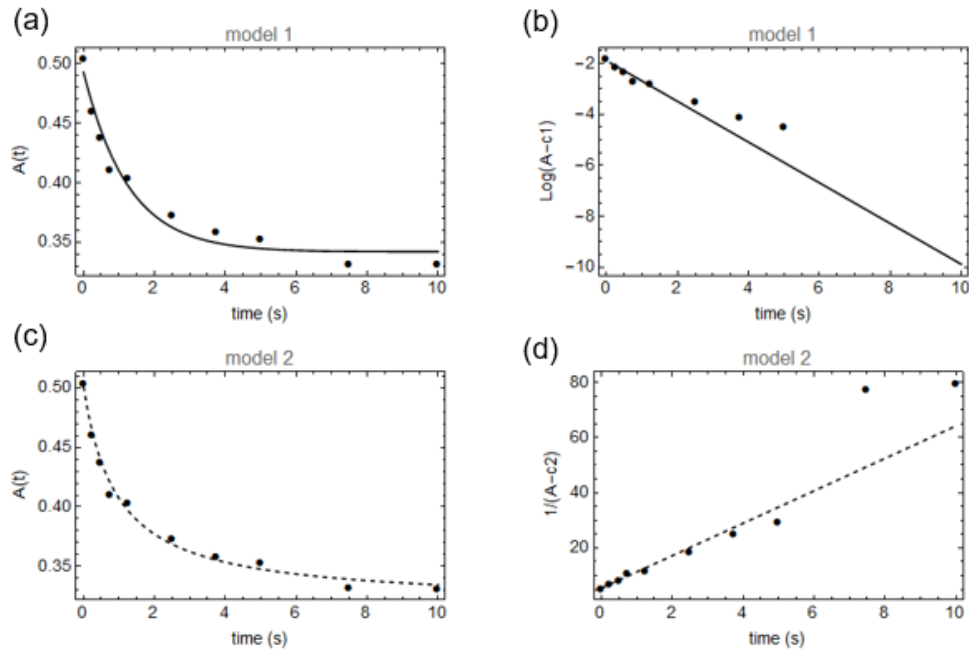


Figure S 3.1: Two models: exponential, model 1, (a) and (b) and hyperbolic, model 2, (c) and (d) of the optical density $A(t)$ interpolations. (a) and (c) represent the linear axes. (b) and (d) represent transformations of Y axis, different for each model, allowing all points collapse to the line – for illustrating the time intervals where each model provides a good approximation.

Both models give similar quality of fit to the experimental data for low exposure i.e. low dose. Both models show poor fits for large exposure times.

SI 3.2 Analysis of asymptotic behavior

The asymptotic behavior of the exponential and hyperbolic mathematical functions representing each fitting model, **Figure S3.2**, indicates that coefficients c for both models corresponds to the optical density of the material at the limit of infinite exposure, $A(t = \infty)$. For the given set of the optical density data both models 1 and 2 give c values quite far from zero, 0.34 and 0.32, respectively.

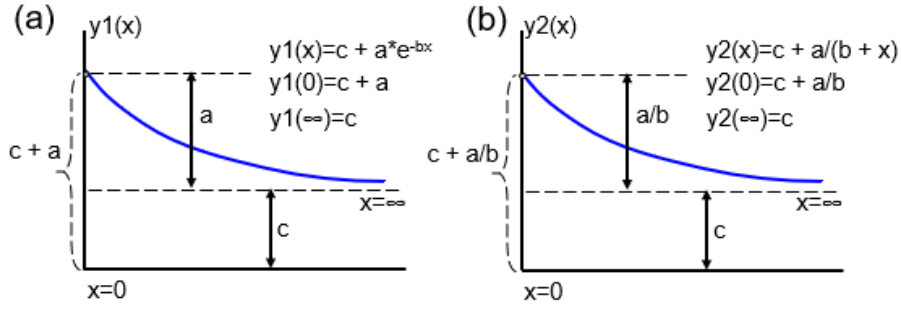


Figure S3.2: Asymptotes at $x \equiv t = \infty$ for both models $y(x) \equiv A(t)$.

Since the optical density is reaching the limit of the decay, the damage is reaching its maximal value and therefore the leftover material in the pad is getting its maximum resistivity to the radiation damage that is being probed in the regime of doses measured.

SI 4. NEXAFS spectra

The C 1s, F 1s and O 1s NEXAFS spectra from a few of the regions in **Fig. 3c** are plotted in **Figures 5(a-c)**. A summary of the peak assignment is presented in **Table S4**. In the undamaged material the peaks at 292.4 and 295.4 eV correspond to the C 1s (CF₂) $\rightarrow \sigma^*_{(C-F)}(\perp)$ and C 1s $\rightarrow \sigma^*_{(C-F)}(\parallel)$ transitions, where the indicated $\sigma^*_{(C-F)}$ orbital is perpendicular and parallel to the main polymer chain, respectively. The shoulder at 298.7 eV peak arises from C 1s (CF₂) $\rightarrow \sigma^*_{(C-C)}(\perp)$ transitions (Ziegler *et al.*, 1994; Castner *et al.*, 1993; Yan *et al.*, 2018). The broad feature at 308 eV is due to C 1s (CF₂) $\rightarrow \sigma^*_{(C-C)}$ transitions. After radiation damage, the peak at 285.2 eV arises from C 1s $\rightarrow \pi^*_{C=C}$ transitions, indicating formation of C=C double bonds after F-loss, while the peak at 287 eV is due to C 1s $\rightarrow \pi^*_{C=O}$ transitions, indicating formation of new C=O bonds (Urquhart & Ade, 2002).

In the undamaged material the F 1s spectrum is dominated by two peaks at 690 and 694 eV, related to the F 1s $\rightarrow \sigma^*_{(F-C)}(\perp)$ and F 1s $\rightarrow \sigma^*_{(F-C)}(\parallel)$ transitions (Yan *et al.*, 2018; Ziegler *et al.*, 1994; Castner *et al.*, 1993). After radiation damage, the intensity of these peaks diminish (with the 690 eV one falling in intensity faster than the 694 eV peak). At large doses these peaks are replaced with one broad F 1s $\rightarrow \sigma^*_{(F-C)}$ peak centered at 693 eV, which reflects the large structural changes in which there are not sufficient numbers of adjacent CF₂ units to form well defined $\sigma^*_{(F-C)}(\perp)$ and $\sigma^*_{(F-C)}(\parallel)$ electronic states.

The peak at 532 eV in the undamaged PFSA is assigned to O 1s \rightarrow $\pi^*_{C=O}$ bonds associated with terminal carboxyl groups (Urquhart & Ade, 2002; Yan *et al.*, 2018). The broad band around 540 eV is associated with O 1s \rightarrow $\sigma^*_{S=O}$ and O 1s \rightarrow σ^*_{C-O} transitions. It is noteworthy that, with increasing dose, the continuum signal in the 536-544 eV range loses intensity much more quickly than the discrete O 1s \rightarrow $\pi^*_{C=O}$ transition at 532 eV. In addition there is a shift of the $\pi^*_{C=O}$ transition to lower energy. This suggests the creation of new C=O bonds, possibly along the main chain, in association with F-loss, with the O coming from either dissociating side-chain sulfonate or ether groups, or from residual O₂ or CO in the STXM tank.

Figure index	Peak #	Energy eV	Edge	Bond	Transition
a	1	285.2	C1s	C=C	$\pi^*(C=C)$
a	2	287	C1s	C=O	$\pi^*(C=O)$
a	3	288.8	C1s		
a	4	292.4	C1s	CF ₂	$\sigma^*(C-F)\perp$
a	5	295.5	C1s	CF ₂	$\sigma^*(C-F)\parallel$
a	6	298.7	C1s	CF ₂	$\sigma^*(C-C)\perp$
a	7	308	C1s	C-C	$\sigma^*(C-C)$
b	1	532	O1s	C=O	$\pi^*(C=O)$
b	2	538	O1s	C-O	$\sigma^*(C-O)$
c	1	690	F1s	CF ₂	$\sigma^*(F-C)\perp$
c	2	694	F1s	CF ₂	$\sigma^*(F-C)\parallel$

Table S4: Energies and assignments of the NEXAFS spectra for the 9-pad experiment

SI 5. Fitting the elemental atomic array, *a*

The following intervals of atomic numbers were used for the iterative fit process: for $1 \leq S \leq 3$, for $1 \leq C \leq 30$, for $1 \leq O \leq 15$ and for $1 \leq F \leq 40$, see **S 1.2**. The initial atomic array was (S=1, C=1, O=1, F=1, H=1), then the atomic numbers for S, C, O, and F were incremented by 1 (or 0.1 depending on expected accuracy), while H was kept set for 1, see **S 1.2**. For all permutations the mean square error (MSE) was calculated, **Eq. S6**. The linear absorption coefficients were calculated for the best elemental arrays corresponding to the interval of the lowest MSE for all pads. **Figure S5** demonstrate how the experimental data of A_i arrays (blue points) align with the product of the calculated linear elemental absorption coefficient on thickness for each pad. Pre and post edge intervals are denoted as (-) and (+), respectively.

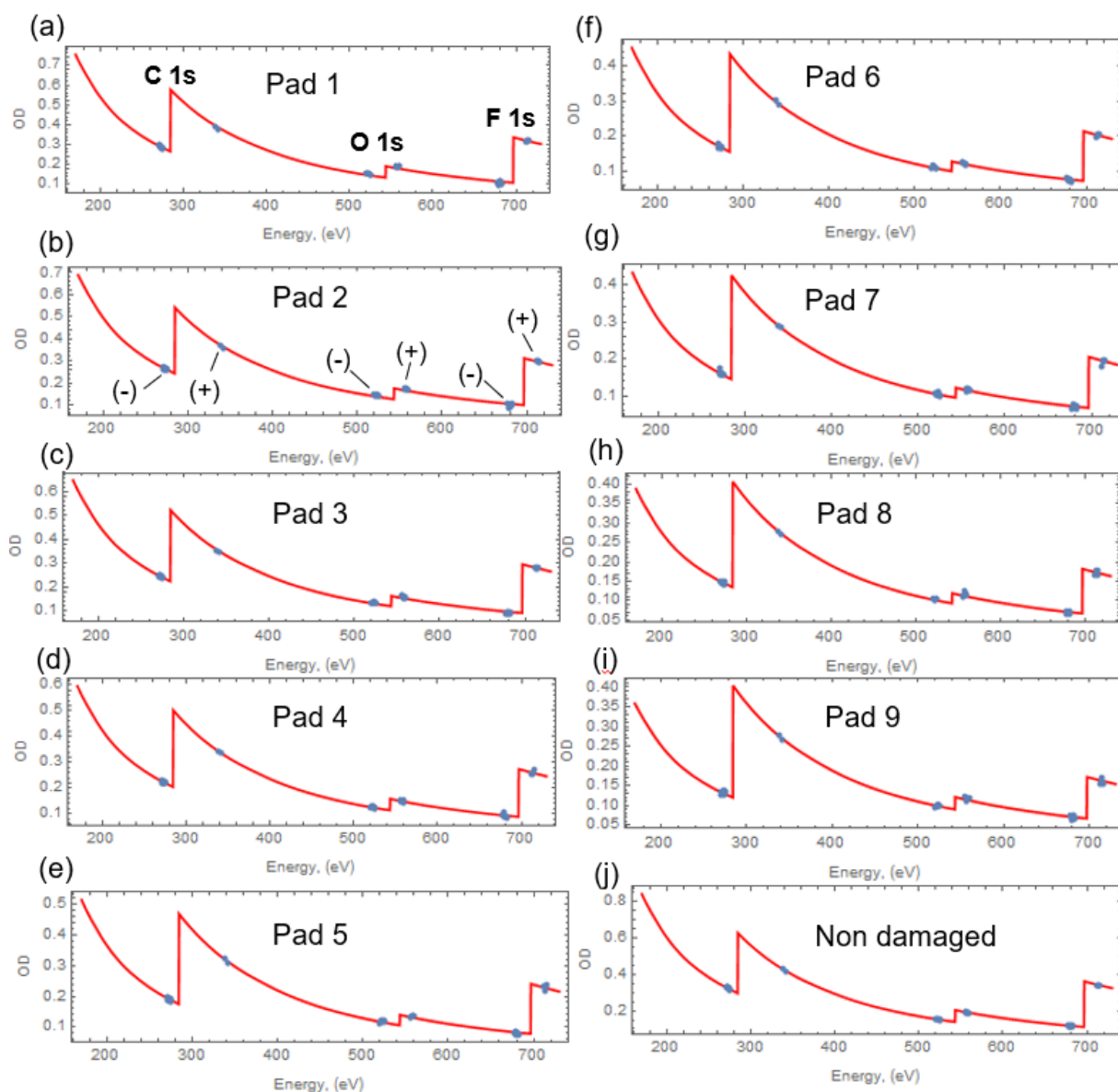


Figure S5 Results of COF optical density fitting of the elemental array \mathbf{a} for 9-pad experiment for PFSA. The panels (a) to (i) plots correspond to the data from 1st (least damaged) to 9th (most damaged) pads, (j) is non damaged area in **Fig. 3c**. Blue points represent series of experimental data from A_i arrays. Red curves are the optical density B_i (traditionally called as OD), which is as a product of the fit linear elemental absorption coefficient and effective thickness, $\mu(\mathbf{a}, e)*h$, calculated for most accurate approximation of the elemental array \mathbf{a} for the given pad.

The numerical compositions of all elemental arrays \mathbf{a} , the least square fit coefficients b and c (according to **Eq.16**) and the corresponding mean square errors (according to **S-1.2 Eq. S10**) are presented in **Table 1** of the main text.

SI 6. Chemical formula of tested PFSA materials

The PFSA material examined (NafionTM D52) is a long side chain (LSC) fluoropolymer with an equivalent weight (EW) of 1100 g/mol. For long side chain PFSA's the formula of the side chain is: $(-\text{OCF}_2-\text{CF}(\text{CF}_3)-\text{O}-\text{CF}_2-\text{CF}_2-\text{SO}_3\text{H})$. For this type of side chain the atomic composition of the repeat molecular unit is defined by the following expression: $\text{S}[1] \text{C}[7+2m] \text{O}[5] \text{F}[13+4m] \text{H}[1]$, see **Scheme 1**, where the value in square brackets is the number of atoms of that type contributing the molecular repeat unit and the quantity $m = (\text{EW}-\text{M}_r(\text{unit}))/\text{M}_r(\text{C}_2\text{F}_4)$, (Mauritz & Moore, 2004). The molecular mass of the repeat unit is $\text{M}_r(\text{unit}) = 444$ g/mol, and the molecular mass of the backbone unit is $\text{M}_r(\text{C}_2\text{F}_4) = 100$ g/mol, making $m=6.56$.

Therefore, the atomic composition of the undamaged NafionTM D52 PFSA is $\mathbf{a} = (1,20,5,39,1)$. *The first position in the atomic composition array is the number of S atoms, second is the number of C atoms, then O atoms, then F atoms, and then H atoms, respectively.* For the iterative fitting procedure, the number of H atoms per repeat unit was always set to 1. This element is not included in the experimental piecewise optical density array \mathbf{A}_i since it has a negligible contribution to the optical density at the X-ray energies used. The S 2p edge was not part of the experimental piecewise optical density array \mathbf{A}_i since as the S 2p signal was not measured reliably. Instead, the number of S atoms per repeat unit in each pad was used as a fitting parameter, since S 2p absorption does contribute significantly to the C 1s pre-edge.

SI 7. Full stack doses

The doses (D_s) received by the sample due to recording the full stacks for the C 1s, O 1s and F 1s edge were calculated according to **Eq. 19** and are summarized in **Table S7**. The full stack analytical study for all 3 edges added about ~ 1 MGy of dose, which is negligible compared to the intentional doses (D_p) used to create analyzable radiation damage see the last column in **Table S7**. The detector efficiency was assumed to be a continuous function of the photon energy $k(e) = (-0.0002e^2 + 0.288e - 32.355)/100$. This interpolation formula was determined from an Excel trend line fit to the data presented in **Figure S2**.

The number of energy points is equal to the number of images in each stack (N_e), the pixel size is 180 nm, the dwell time is 1 ms, the material density is 2 g/cm³, the linear absorption coefficient μ is calculated based on the elemental array for each pad determined by fitting the re- and post-edge signals.

Pad #	Doses, D_s (MGy)				Dp (MGy)
	C1s	O1s	F1s	Total	Model #4
1	0.28	0.27	0.23	0.77	1.4E+01
2	0.28	0.27	0.23	0.78	2.8E+01
3	0.28	0.28	0.23	0.79	4.3E+01
4	0.29	0.29	0.24	0.82	7.3E+01
5	0.30	0.30	0.24	0.84	1.5E+02
6	0.31	0.31	0.24	0.86	2.3E+02
7	0.31	0.31	0.24	0.87	3.2E+02
8	0.33	0.33	0.25	0.91	5.0E+02
9	0.31	0.33	0.23	0.87	6.8E+02

Table S7: Full stack doses D_s per each pad for C1s, O1s, and F1s edges in comparison with the intentionally applied doses D_p .

SI 8. Functional fitting of molecular mass, M_r , and areal density, ρ^*h , of the pads

The analysis was performed on the data points presented in **Fig. 9b** and **Fig. 11**. Similarly, as for (SI 3.1), two models of interpolation were used: exponential and hyperbolic. Model 1 uses an exponential interpolation $y(t) = c_1 + a_1 e^{-b_1 t}$. Model 2 uses a hyperbolic interpolation $y(t) = c_2 + \frac{a_2}{b_2 + t}$. The least linear square fit was applied for both test functions M_r and ρ^*h .

SI 8.1 Molecular mass M_r (Fig. 9)

In **Figure S8.1** the exponential fit corresponds to the solid curve, and the hyperbolic fit to the dashed curve. It is clear that the exponential function provides the better fit; its mean square error, MSE, is ~ 10 times lower than for the hyperbolic fit. It is interesting to note that the best fitting of the exponential function was for the pads with the highest doses, i.e. for pads 7, 8, 9. The hyperbolic function *does not fit* for the whole available M_r data interval.

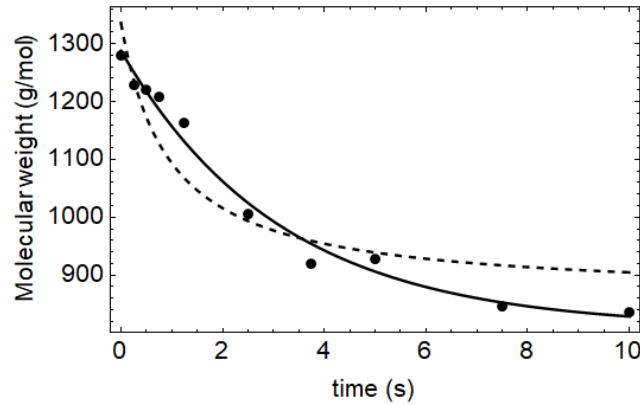


Figure S8.1: Least linear square fitting of M_r data against the exponential (solid) and hyperbolic (dashed) approximations.

Table S 8.1 presents the fitting coefficients and mean square error, MSE, calculated for each model with respect to the given data points of $M_r(t)$.

	a	b	c	MSE
model 1	4.8E+02	0.32	8.1E+02	1.40E+03
model 2	4.5E+02	0.95	8.6E+02	1.09E+04

Table S 8.1. Least linear fitting coefficients for models 1 and 2 applied for $M_r(t)$ data in **Fig. 9b**

SI 8.2 Areal density $\rho \cdot h$ (Fig .11)

For clarity, the fitting of areal density is presented in linear (left) and log-log (right) scales. In contrast to the fits for M_r , the hyperbolic fit to the areal density $\rho \cdot h$ is significantly better than the exponential one. The exponential approximation produces the highest misfit for very small and very large radiation damages.

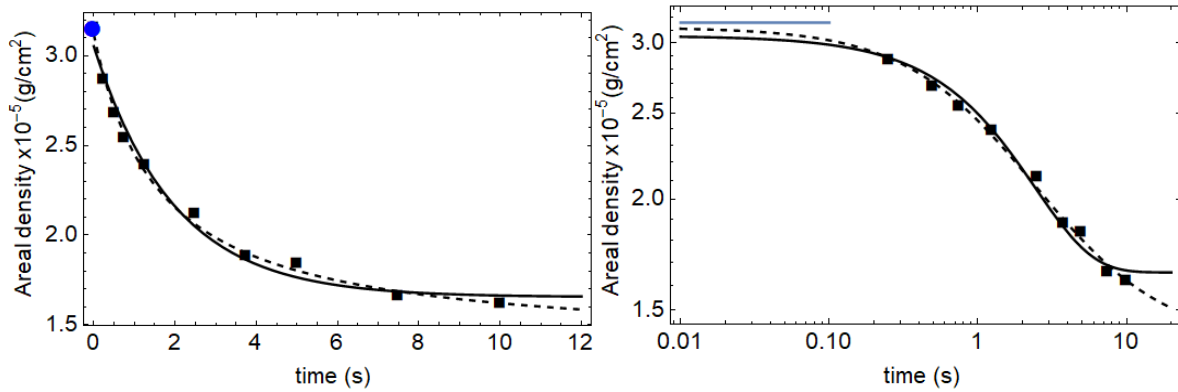


Figure S8.2: Least linear square fitting of $\rho*h$ data in **Fig. 11** against the exponential (solid) and hyperbolic (dashed) approximations. Blue point (linear) and blue line (log-log) corresponds to undamaged sample.

The overall error, MSE, is also significantly higher for the exponential (model-1) approximation.

	a	b	c	MSE
model 1	1.4	0.5	1.7	1.1 E-02
model 2	2.8	1.6	1.4	3.4 E-03

Table S8.2: Least linear fitting coefficients for models 1 and 2 applied for $\rho*h$ data in **Fig. 11**

SI 9. Relationship between elemental optical density and linear absorption coefficient spectra

The composition of the material is a function of the applied dose, **Fig. 9a**, so the linear absorption coefficients, **Fig. 10a**, vary systematically with the dose. However, the elemental linear absorption coefficient for each pad varies most at the C 1s edge and least at the F 1s edge. At first, this observation does not seem to make sense, since the measured C 1s edge jump varies very little over the set of damaged pads whereas the F 1s edge jump drops precipitously with increasing dose - see **Fig. 5** and **Fig. 8**. The dose dependence of the linear absorption coefficients (**Fig.10a**) can be reconciled with the measured spectra when one takes into account the changing thickness of the pads due to radiation damage. The elemental optical density A is proportional to both the pad thickness and the pad linear absorption coefficient, $A=\mu*\rho*h$. For this data set we do not have thickness, h , as a measured independent parameter. However, for illustration

purposes, we will assume that the density of the damaged pads changes much less than the thickness and therefore, assume the density to be the same as that of undamaged PFSA, 2.0 g/cm^3 . Thus, the pad geometric thickness (h) in nm is given by $100 \cdot (\text{areal density in } 10^{-5} \text{ g/cm}^2) / (\text{density in } \text{g/cm}^3)$; the derived thickness values are summarized in **Table 1**.

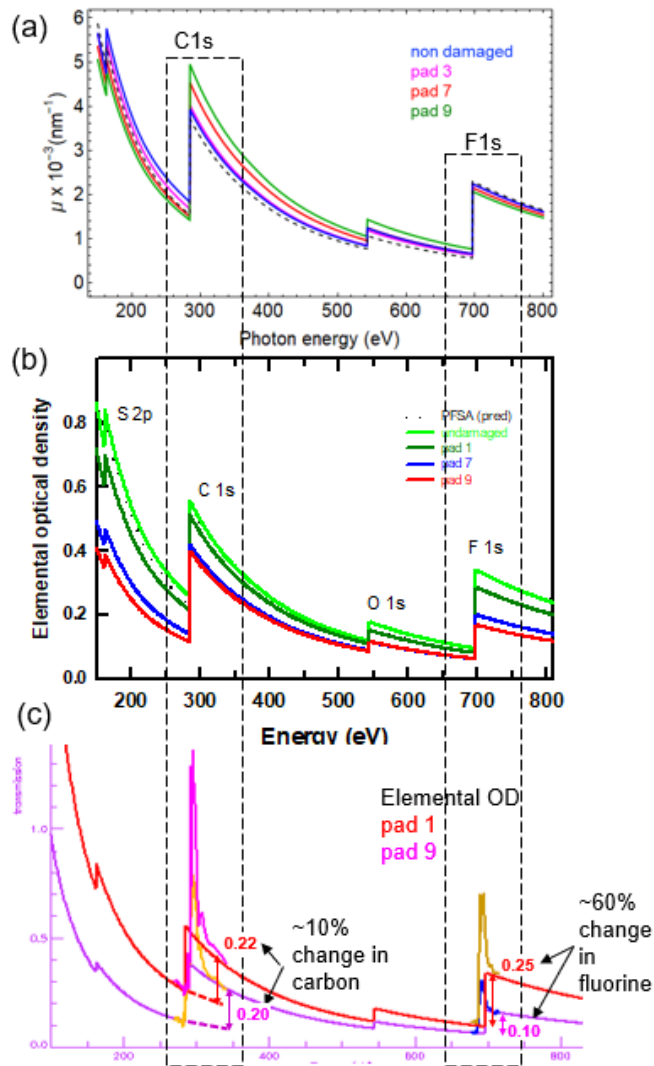


Figure S-9: Comparing the spectra of the calculated linear absorption coefficient μ , (a); the elemental optical density $A = \mu \cdot h$, (b); and the experimental optical density (c). The colors of curves are independent for each panel. Two edges are selected for comparison C 1s and F 1s.

Fig. S-9b plots the product of the elemental linear absorption coefficient and the thickness for the undamaged material for the pad 1, pad 7 and pad 9. Once the reduction in pad thickness is taken into account, one sees that the spectral (and compositional) changes are largest at the F 1s

edge, which drops by more than 60% between pads 1 and 9, while the C 1s contribution (as measured by the C 1s edge jump) barely changes (~10%). The pre C1s signal decreases by a very large amount, which is consistent with the large fluorine loss since the signal below 280 eV is dominated by the valence ionization continuum of fluorine. **Fig. S-9c** plots the optical density spectra for pad 1 and pad 9, in comparison to the elemental spectra, $\mu^* \rho^* h$, calculated for the two pads, using the methods outlined in this article. It is clear that the method does accurately reproduce the well-known behavior of X-ray damaged PFSA, namely a very rapid decrease in the F 1s signal (both edge jump and spectral fine structure), associated with fluorine loss, but very little change in the C 1s edge jump.

SI References

- Castner, D. G., Lewis, K. B., Fischer, D. A., Ratner, B. D. & Gland, J. L. (1993). *Langmuir*. **9**, 537–542.
- Henke, B. L., Gullikson, E. M. & Davis, J. C. (1993). *At. Data Nucl. Data Tables*. **54**, 181–342.
- Leontowich, A. F. G., Hitchcock, A. P., Tyliczszak, T., Weigand, M., Wang, J. & Karunakaran, C. (2012). *J. Synchrotron Radiat*. **19**, 976–987.
- Mauritz, K. A. & Moore, R. B. (2004). *Chem. Rev.* **104**, 4535–4586.
- Urquhart, S. G. & Ade, H. (2002). *J. Phys. Chem. B*. **106**, 8531–8538.
- Yan, Z. B., Hayes, R., Melo, L. G. A., Goward, G. R. & Hitchcock, A. P. (2018). *J. Phys. Chem. C*. **122**, 3233–3244.
- Ziegler, C., Schedel-Niedrig, T., Beamson, G., Clark, D. T., Salaneck, W. R., Sotobayashi, H. & Bradshaw, A. M. (1994). *Langmuir*. **10**, 4399–4402.